inorganics

MDPI

Article

Nitrogen-Doped Carbon Flowers with Fe and Ni Dual Metal Centers for Effective Electroreduction of Oxygen

Rene Mercado, Forrest Nichols and Shaowei Chen *

Department of Chemistry and Biochemistry, University of California, 1156 High Street, Santa Cruz, CA 95064, USA; rsmercad@ucsc.edu (R.M.); fnichols@ucsc.edu (F.N.)
* Correspondence: shaowei@ucsc.edu

Abstract: Carbon-based nanocomposites have been attracting extensive attention as high-performance catalysts in alkaline media towards the electrochemical reduction of oxygen. Herein, polyacrylonitrile nanoflowers are synthesized via a free-radical polymerization route and used as a structural scaffold and precursor, whereby controlled pyrolysis leads to the ready preparation of carbon nanocomposites (FeNi-NCF) doped with both metal (Fe and Ni) and nonmetal (N) elements. Transmission electron microscopy studies show that the FeNi-NCF composites retain the flower-like morphology, with the metal species atomically dispersed into the flaky carbon petals. Remarkably, despite a similar structure, elemental composition, and total metal content, the FeNi-NCF sample with a high Fe:Ni ratio exhibits an electrocatalytic performance towards oxygen reduction reaction (ORR) in alkaline media that is similar to that by commercial Pt/C, likely due to the Ni to Fe electron transfer that promotes the adsorption and eventual reduction of oxygen, as evidenced in X-ray photoelectron spectroscopic measurements. Results from this study underline the importance of the electronic properties of metal dopants in the manipulation of the ORR activity of carbon nanocomposites.

Keywords: polyacrylonitrile; carbon flower; metal–metal charge transfer; electrocatalytic activity; oxygen reduction reaction

Citation: Mercado, R.; Nichols, F.; Chen, S. Nitrogen-Doped Carbon Flowers with Fe and Ni Dual Metal Centers for Effective Electroreduction of Oxygen. *Inorganics* **2022**, *10*, 36. https://doi.org/10.3390/inorganics10030036

Academic Editor: Raymond J. Gorte

Received: 12 February 2022
Accepted: 10 March 2022
Published: 11 March 2022

1. Introduction

The development of sustainable energy technologies has been attracting extensive interest, and fuel cells represent a unique viable option [1]. Typical fuel cell operation entails two main reactions, the oxidation of small-molecule fuels at the anode and the reduction of oxygen at the cathode, where appropriate catalysts are needed to generate a current density sufficiently high for practical applications. These are, in general, based on the platinum group metals (PGM). Nevertheless, the precious nature of PGM has significantly impeded the commercial implementation of these technologies [2]. In addition, PGM-based catalysts are prone to inactivation by poisoning species (e.g., CO) and structural instability due to Ostwald ripening in long-term operation, which compromises their overall performance [3,4]. Thus, significant efforts have been dedicated to the development of alternative catalysts, in particular, for the cathodic oxygen reduction reaction (ORR), which has been largely accepted as a significant roadblock limiting fuel cell performance. Among these, carbon-based nanocomposites have been recognized as viable electrocatalysts, mostly owing to ready structural engineering that renders it possible to obtain a large surface area, good electrical conductivity, corrosion resistance, and a skeleton that is easy to modify for both functionalization and heterodoping [5–7]. For instance, heteroatoms such as nitrogen and sulfur can be readily doped into the carbon matrices, leading to electron redistribution and an activation of various atomic sites that is conducive to the adsorption of key ORR intermediates. Thus, doped carbon can exhibit an apparent ORR activity, although it is typically inferior to that of the commercial Pt/C benchmark [8,9]. Performance improvements can be achieved with the additional doping of select metal centers, forming

MN_x coordination moieties [10–14]. This is primarily attributed to the synergistic tuning of the electronic interactions between the MN_x sites and reaction intermediates [15]. In fact, extensive research has been reported on metal–nitrogen co-doped carbon since the first breakthrough with a Fe–N–C catalyst in 2009 [6,7,16]. However, it has been recognized that the binding strength of the FeN_x moiety to oxygen is somewhat too strong, and an electron-deficient environment is preferred for the further enhancement of the ORR performance. One effective strategy is to incorporate a second metal center to manipulate the electronic property of the FeN_x site [17].

Indeed, in recent years, carbon nanocomposites with bimetal dopants have been found to exhibit further improved ORR activity, in comparison to the mono-metal based counterparts, largely due to the unique metal–metal charge transfer that provides a further control of the electronic interactions with ORR intermediates [18,19]. For instance, carbon nanocomposites doped with Fe/Co [20], Fe/Mn [21], and Fe/Ni [22] have shown a remarkable ORR activity. The enhanced performance can also be aided by the formation of a three-dimensional (3D) porous carbon scaffold, with interconnected micropores, mesopores, and macropores that facilitate both the electron transfer involved in ORR and the mass transfer of reactants and electrolyte species.

Herein, polyacrylonitrile with a nanoflower morphology was first prepared by free radical polymerization [23], and was transformed into N-doped carbon nanoflowers embedded with Fe/Ni bimetallic centers by controlled pyrolysis with the addition of iron and nickel compounds at varied feeds. It was found that the obtained nanocomposites displayed a significantly improved ORR activity in alkaline media, in comparison to the metal-free or monometal counterparts, signifying the critical role of the metal dopants in dictating the electrocatalytic activity, and of the nanoflower morphology in facilitating accessibility to the electrocatalytic active sites and mass transport of key reaction species.

2. Results and Discussion

Polyacrylonitrile was first prepared by azobis(isobutyronitrile) (AIBN)-initiated free radical polymerization of acrylonitrile, exhibiting a nanoflower morphology with a diameter of ca. 850 nm and porous petals [23], as manifested in transmission electron microscopy (TEM) measurements (Figure S1a). The overall morphology was stabilized in a subsequent thermal annealing in ambient air at 230 °C, but with a slight shrinkage of the nanoflowers to ca. 750 nm (Figure S1b), suggesting the increasing rigidity and compactness of the polymer flowers [24]. Note that this stabilization step was critical to preserve the nanoflower structure after pyrolysis. Upon carbonization at 900 °C (Figure S1c), one can see that carbon nanoflowers (NCF) were produced, but that the size was further decreased to 400–500 nm [25]. A similar structure was observed for the Fe/Ni-codoped carbon nanocomposites, which were prepared by soaking the polyacrylonitrile nanoflower precursors in an aqueous solution containing $FeCl_3$ and $Ni(NO_3)_2$ at a total concentration of 3 mM, but at varied feed ratios of 1:0, 1:1, 2:1, and 3:1 prior to pyrolysis at 900 °C. The obtained samples were denoted as Fe-NCF and FeNi-NCF(1,2,3), respectively. From Figure 1a, the FeNi-NCF(3) sample can be seen to retain the flower morphology with a diameter of ca. 400 nm. Furthermore, at higher magnifications, no particulates can be identified within the flaky petals, suggesting that the metal species were atomically distributed within the carbon scaffolds (Figure 1b); furthermore, the nanoflowers entailed only short-range lattice fringes, featuring an interplanar separation of ca. 0.34 nm (Figure 1c), suggestive of the formation of highly defective carbon. In fact, from the elemental maps acquired with energy-dispersive X-ray spectroscopy (Figure 1d–g), one can see a rather uniform distribution of Fe, Ni, and N over the C background.

The sample structures were further characterized by X-ray diffraction (XRD) measurements (not shown), where only two broad peaks were identified at $2\theta \approx 21^\circ$ and 41°, due to the (002) and (101) facets of graphitic carbon, respectively (PDF card #65-6212), confirming the successful carbonization of polyacrylonitrile. No diffraction features characteristic of

metal/metal oxide nanoparticles can be resolved, consistent with atomic dispersion of the metal species into the carbon matrix.

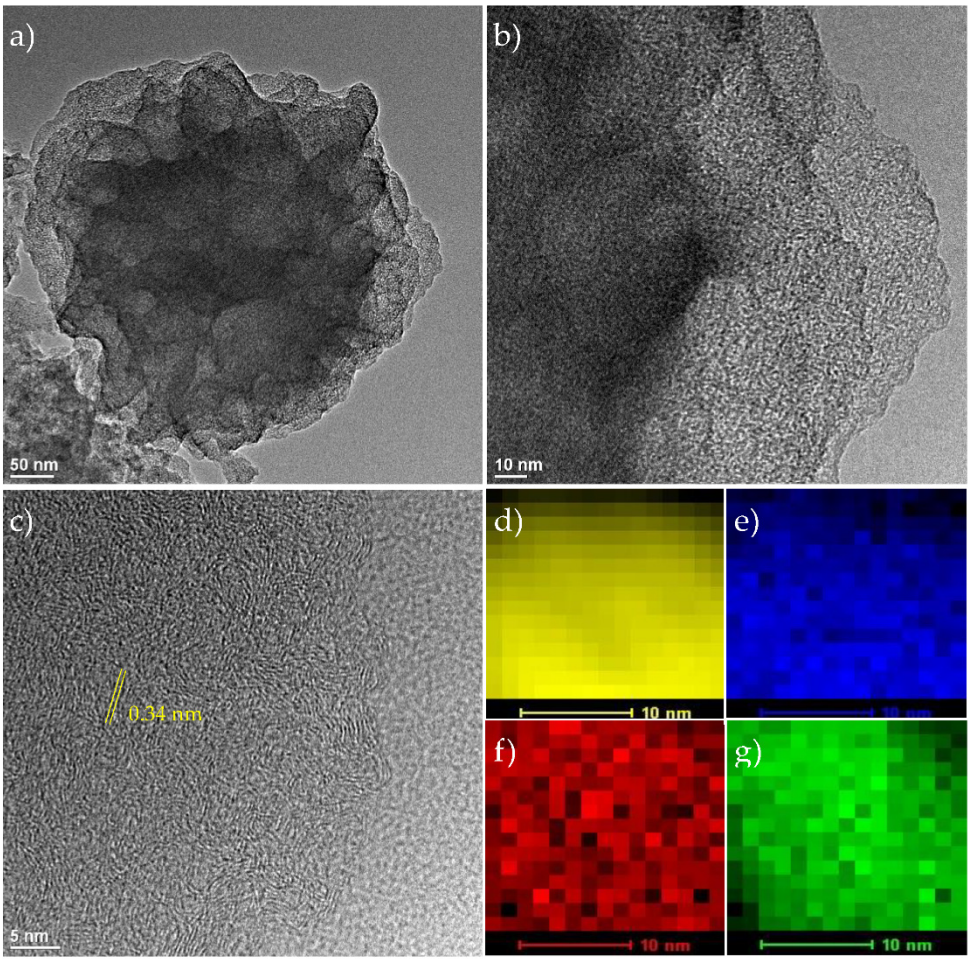

Figure 1. (**a**–**c**) TEM images of FeNi-NCF(3) at different magnifications, along with the associated elemental maps of (**d**) C, (**e**) N, (**f**) Fe, and (**g**) Ni.

The sample porosity was then examined by nitrogen sorption measurements (Figure 2). From panel a, the metal-free NCF can be seen to display a Type-I nitrogen adsorption/desorption isotherm with a hysteresis loop, which suggests mostly micropores, whereas FeNiC-NCF(3) produced a Type-IV isotherm, suggesting the formation of both micropores and mesopores in the sample. From the pore size distributions (panel b), NCF was indeed found to consist mostly of micropores of ca. 1.25 nm, whereas FeNi-NCF(3) contained a significant portion of mesopores at 2.5 nm, likely due to the thermal volatility of the metal compounds that renders them effective porogens [5]. Additionally, the Brunauer–Emmett–Teller (BET) specific surface area was found to increase from 90 m^2 g^{-1} for NCF to 110 m^2 g^{-1} for FeNi-NCF(3).

X-ray photoelectron spectroscopy (XPS) measurements were then carried out to evaluate the elemental composition and valency of the nanocomposites. Figure S2 (Supplementary Materials) shows the survey spectra, where the elements of carbon, nitrogen, and oxygen can be clearly resolved within the NCF, Fe-NCF, and FeNi-NCF samples, with additional Fe and Ni for the latter, indicative of the successful doping of the carbon skeletons by N, Fe, and Ni. On the basis of the integrated peak areas, the metal-free NCF sample was found to consist of 90.11 at% of C, 6.20 at% of N and 3.70 at% of O. The Fe-NCF sample consisted of 92.2 at% of C, 2.28 at% of N, 0.13 at% of Fe, and 5.41 at% of O. In the FeNi-NCF series, the carbon content stayed virtually invariant at ca. 90 at%; the N content was about 2.28 at% for Fe-NCF, 2.21 at% for FeNi-NCF(1), 4.09 at% for FeNi-NCF(2), and 4.10 at% for

FeNi-NCF(3); the O content increased somewhat to 6.97 at% for FeNi-NCF(1), 6.10 at% for FeNi-NCF(2), and 4.41 at% for FeNi-NCF(3), suggesting that the basic carbon scaffold was almost unchanged with the addition of the metal precursors (Table S1). Notably, the total metal content remained low among the Fe-NCF and FeNi-NCF samples, only 0.15 at% for Fe-NCF, 0.26 at% for FeNi-NCF(1), 0.27 at% for FeNi-NCF(2), and 0.22 at% for FeNi-NCF(3), with a respective Fe:Ni atomic ratio of 1.0, 2.0, and 3.5 for the FeNi-NCF series, which is in rather good agreement with the initial feeds.

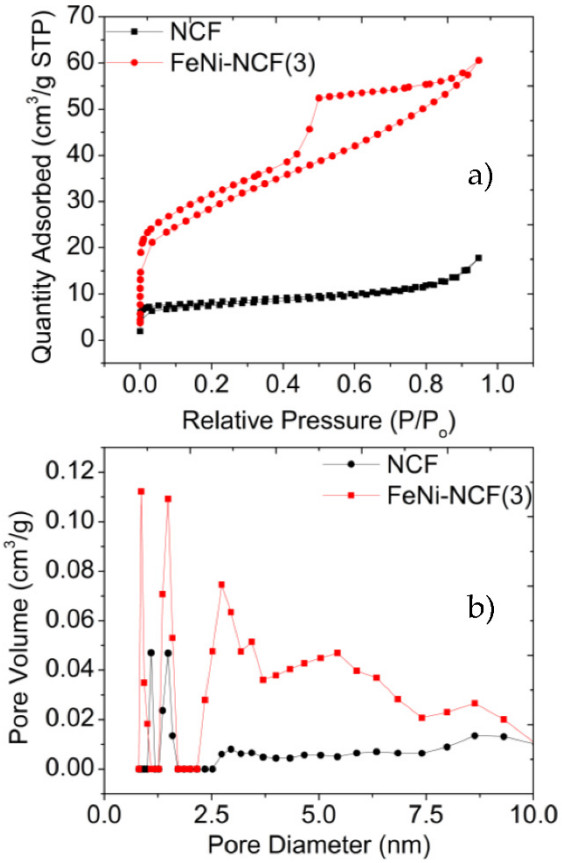

Figure 2. (**a**) N_2 sorption isotherms and (**b**) the corresponding pore size distributions of NCF and FeNi-NCF(3).

The high-resolution C 1s spectra are shown in Figure S3, where the FeNi-NCF samples all displayed a major component at 284.4 eV due to graphitic sp^2 carbon, evidence of the successful carbonization of polyacrylonitrile, C sp^3 at 285.1 eV, with two minor ones at 286.7 and 289.7 eV, corresponding to oxidized carbon such as C=O and COOH, respectively [26]. The corresponding N 1s, O 1s, Fe 2p, and Ni 2p spectra for Fe-NCF and FeNi-NCF are depicted in Figures 3 and S4. From the N 1s spectra in Figure 3a, six N species can be resolved at ca. 398.1 eV for pyridinic N, 398.9 eV for metal–N, 399.9 eV for pyrrolic, 400.8 eV for graphitic, 401.7 eV for oxidized N, and 403 eV for NO_2 [27,28]. Note that the metal–N peak was absent in the NCF sample (Figure S5). The O 1s spectra are shown in Figure 3b, which contain three components, 532.2 eV for O–C, 533.3 eV for O–H, and 530.1 eV for metal–O [29,30]. These results collectively indicate that the metal species are most likely involved in the chelation interactions with the N and O dopants within the carbon skeletons.

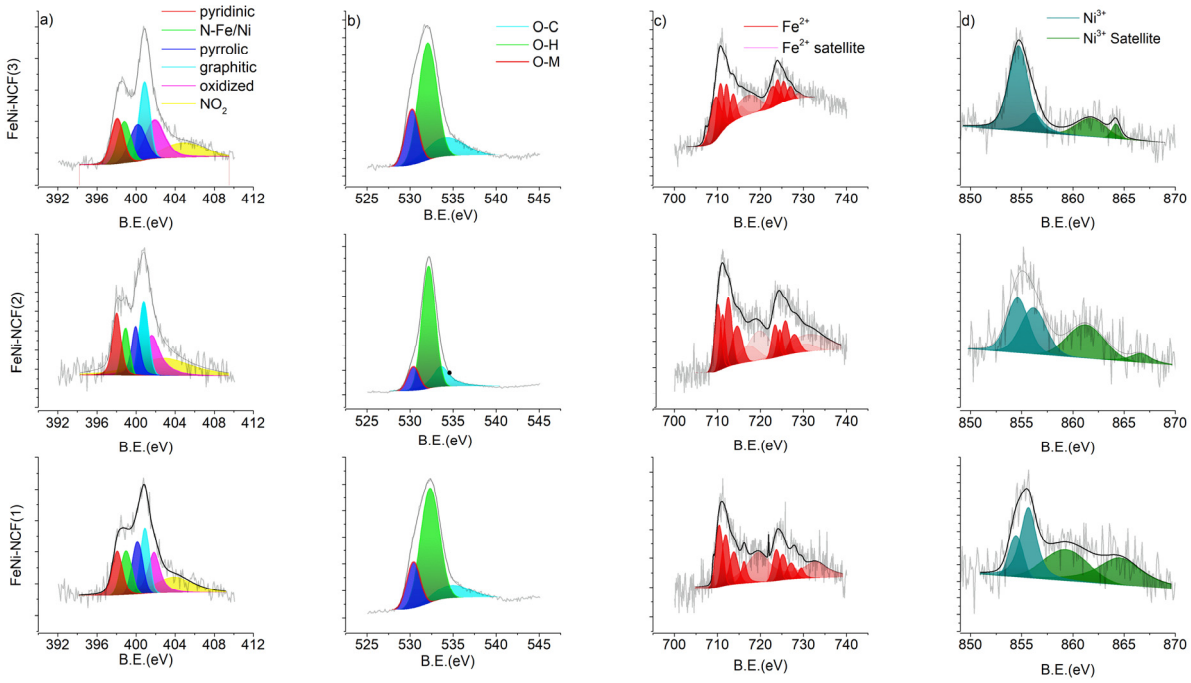

Figure 3. High-resolution XPS spectra of the FeNi-NCF samples: (**a**) N 1s, (**b**) O 1s, (**c**) Fe 2p, and (**d**) Ni 2p.

From the Fe 3p spectra in Figures 3c and S4, it can be seen that the FeNi-NCF and Fe-NCF samples all displayed a very consistent binding energy of the Fe $2p_{3/2}$ electrons at about 710 eV, which can be ascribed to Fe^{2+}. Similarly, from the Ni 2p spectra in Figure 3d, the FeNi-NCF samples can be seen to show a binding energy of ca. 854.6 eV for the $2p_{3/2}$ electrons of Ni^{2+} [18,31]. Interestingly, one can see that among the series, the FeNi-NCF(3) sample showed the lowest binding energy for Fe $2p_{3/2}$ at 709.58 eV, but the highest binding energy for Ni $2p_{3/2}$ at 854.69 eV, suggesting that the Fe^{2+} centers were in an electron-withdrawing environment (Table S2) [18,32]. Note that such Ni to Fe metal–metal charge transfer is conducive to ORR electrochemistry catalyzed by metal-doped carbon nanocomposites (vide infra) [33,34].

The ORR activity of the nanocomposites was then evaluated and compared in alkaline media. As shown in Figure 4a, the nanocomposite samples all exhibited a non-zero ORR activity in 0.1 M KOH; however, the activity varied among the samples. It can be seen that the metal-free NCF exhibited only a minimal activity featuring an onset potential (E_{onset}) below +0.6 V. The activity was substantially improved with the Fe-NCF sample, with E_{onset} = +0.89 V and (half-wave potential) $E_{1/2}$ = +0.72 V, signifying the key role of metal species in driving the electron-transfer kinetics. The performance was further enhanced with the FeNi-NCF samples, and FeNi-NCF(3) exhibited the best activity within the series, where the $E_{1/2}$ (+0.79 V) and E_{onset} (+0.93 V) values were only somewhat lower than those of the commercial Pt/C benchmark ($E_{1/2}$ = +0.83 V, E_{onset} = +1.00 V).

The electron-transfer number (n) and H_2O_2 yield (H_2O_2%) were then estimated from the RRDE data (Figure 4b). Again, FeNi-NCF(3) exhibited the best performance, with the higher n and lower H_2O_2% than all other samples. For example, at +0.70 V, the n/H_2O_2% values were 3.99/0.59 for FeNi/NCF(3), in comparison to 3.82/9.6 for FeNi/NCF(2), 3.87/7.1 for FeNi/NCF(1), 3.99/0.69 for Fe-NCF, and 3.99/0.4 for Pt/C, indicating high selectivity of the $4e^-$ ORR pathway by the nanocomposites. Figure 4c shows the associated Tafel plots, where FeNi-NCF(3) exhibits the lowest slope of 77.62 mV dec^{-1}, which suggested that the first electron reduction of oxygen was likely the rate-limiting step [33,34].

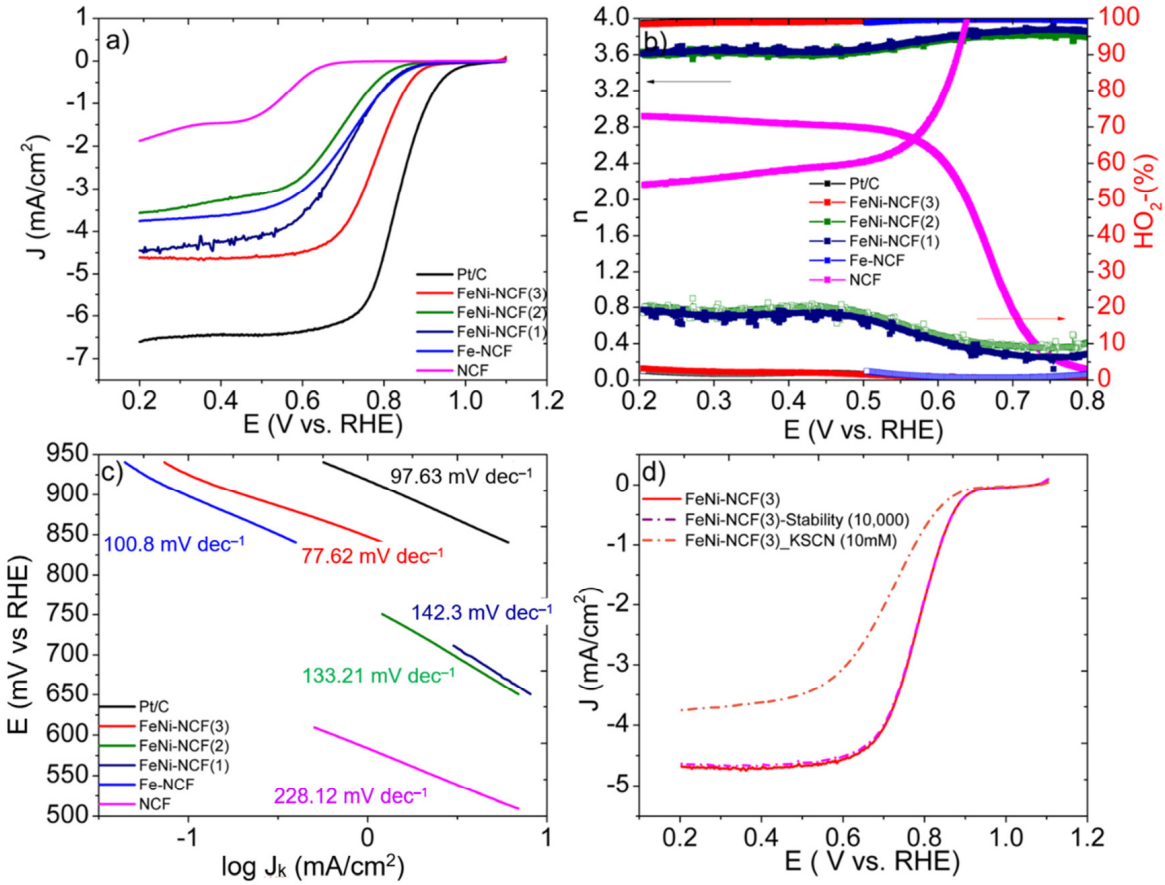

Figure 4. (**a**) ORR polarization curves of the sample series in an oxygen-purged 0.1 M KOH solution. Potential sweep rate 10 mV s^{-1}, rotation rate 1600 rpm. (**b**) Electron transfer number (left *y*-axis) and H_2O_2% yield (right *y*-axis) for the electrocatalysts in (**a**), and (**c**) the corresponding Tafel plots. (**d**) ORR polarization curves in the first scan and after 10,000 potential cycles within +0.2 to +1.1 V, as well as with the introduction of KSCN (10 mM).

As mentioned earlier, the FeNi-NCF sample series consisted of a similar elemental composition and total metal contents (Table S1). Therefore, it is most likely that the remarkable ORR activity of FeNi-NCF(3) is a consequence of the collective contributions of a porous structure that promoted transport of electrolyte ions and reaction species, as well as effective Ni–Fe charge transfer that facilitated the adsorption and ultimately reduction of oxygen, where the reduced electron density of the Fe centers led to a weakened interaction with oxygen intermediate, a unique feature favored for ORR electrocatalysis [33,34].

Notably, the FeNi-NCF(3) sample also exhibited remarkable stability. The ORR polarization curve remained virtually unchanged after 10,000 potential cycles within the range of +0.20 to 1.00 V (Figure 4d). However, the introduction of KSCN (10 mM) led to a substantial diminishment of the ORR activity (Figure 4d), due to blocked access to the catalytic active sites, further confirming the key role of the metal species in ORR electrocatalysis.

3. Materials and Methods

3.1. Chemicals

Iron(III) chloride ($FeCl_3$, 97%, Sigma Aldrich, St. Louis, MO, USA), nickel(II) nitrate ($Ni(NO_3)_2$, 99.999%, Sigma Aldrich, St. Louis, MO, USA), azobis(isobutyronitrile) (AIBN, 98%, Sigma Aldrich, St. Louis, MO, USA), acrylonitrile (≥99%, Sigma Aldrich, St. Louis, MO, USA), and Pt/C (20 wt%, Alfa Aesar, Ward Hill, MA, USA) were used as received without further treatment. Water was purified with a Barnstead Nanopure Water system (resistivity 18.3 MΩ cm).

3.2. Sample Preparation

Polyacrylonitrile with a nanoflower morphology was first prepared by following a free radical polymerization procedure reported previously with modification [23]. Briefly, 4 mL of acrylonitrile was dispersed into 4 mL of acetone, into which was then added 4 mL of AIBN as the initiator. The reaction was run for 2 h in a vial at 70 °C, affording a white powder (PACN-70) after being dried at ambient temperature for 1 d. The sample was then stabilized by thermal treatment in air at 230 °C for 2 h, producing a brown powder denoted as PACN-230.

The obtained PACN-230 was then utilized to prepare Fe/Ni-codoped carbon flowers. Briefly, 20 mg of PACN-230 was sonicated in acetone for 45 min, into which was then added an aqueous solution containing $FeCl_3$ and $Ni(NO_3)_2$ with a total concentration of 3 mM but at varied feed ratios: 1:0, 1:1, 2:1, and 3:1. The mixture was then dried in vacuum, loaded into a tube furnace, and thermally treated at 900 °C in a N_2 atmosphere for 1 h. The produced black powders were referred to as Fe-NCF and FeNi-NCF(1,2,3), respectively. A control sample (NCF) was also synthesized in the same fashion but in the absence of any metal salts.

3.3. Characterization

Transmission electron microscopic (TEM) images were acquired with an aberration-corrected Titan FEI electron microscope. Nitrogen sorption isotherms were obtained at 77 K using 99.999% N_2 with an Autosorb iQ2 (Quantachrome) low-pressure gas sorption analyzer. X-ray diffraction (XRD) patterns were acquired with a Bruker D8 Advance diffractometer with Cu K_α radiation (λ = 0.15418 nm). X-ray photoelectron spectroscopic (XPS) studies were performed with a PHI 5000 Versaprobe instrument.

3.4. Electrochemical Tests

Electrochemical studies were all performed in a three-electrode configuration with a CHI 710 electrochemical workstation. The counter electrode was a graphite rod, while a Ag/AgCl electrode in 1.0 M KCl served as the reference electrode. A reversible hydrogen electrode (RHE) was used to calibrate the potential of the reference electrode, and the potentials in the present study were all referenced to this RHE. The working electrode was a gold ring–glassy-carbon disk electrode (RRDE) purchased from Pine Research Instrumentation. In the preparation of catalyst inks, the nanocomposites prepared above (0.8 mg) and a Nafion solution (20%, 2.0 μL) were added to a mixture of water and ethanol (1:1 *v:v*, 200 μL). After 30 min of sonication, a calculated amount of the ink (5.0 μL) was cast onto the glassy-carbon disk. The loading of the catalysts was estimated to be 84.2 μg cm^{-2}. After the catalyst film was dried, it was covered with 3.0 μL of 20% Nafion, and the electrode was introduced into the electrolytes for electrochemical measurements.

4. Conclusions

In this study, carbon nanoflowers doped with both metal (Fe and Ni) and non-metal (N) elements were readily synthesized by the controlled pyrolysis of polyacrylonitrile flowers in the presence of Fe and Ni compounds. The obtained FeNi-NCF nanocomposites exhibited a similar elemental composition and total metal content. However, the sample that exhibited a high Fe:Ni atomic ratio showed the best ORR performance, close to that of commercial Pt/C, likely due to the Ni to Fe metal–metal charge transfer that facilitated the adsorption and, ultimately, the reduction of oxygen, as evidenced in XPS measurements. Results from this study suggest that structural engineering of the electronic properties of metal dopants is a critical strategy for improving the electrocatalytic activity of carbon-based nanocomposites.

Supplementary Materials: The following supporting information can be downloaded at: https://www.mdpi.com/article/10.3390/inorganics10030036/s1, Figure S1: TEM images of (a) PACN-70, (b) PACN-230, and (c) NCF; Figure S2: XPS survey spectra of FeNi-NCF(1), FeNi-NCF(2), FeNi-

NCF(3), and NCF; Figure S3: High-resolution C 1s spectra of the series of FeNi-NCF samples; Figure S4: High-resolution scans of the (a) C 1s, (b) N 1s, and (c) Fe 2p electrons of Fe-NCF; Figure S5: High-resolution XPS scans of the (a) C 1s and (b) N 1s electrons of NCF; Table S1: Elemental compositions of the sample series from XPS measurements; Table S2: Binding energies of Fe and Ni in the sample series from XPS measurements.

Author Contributions: Conceptualization, S.C.; methodology, S.C.; formal analysis, R.M.; investigation, R.M. and F.N.; resources, S.C.; data curation, R.M. and F.N.; writing—original draft preparation, R.M. and F.N.; writing—review and editing, S.C.; supervision, S.C.; project administration, S.C.; funding acquisition, S.C. All authors have read and agreed to the published version of the manuscript.

Funding: This research was funded by the US National Science Foundation, grant numbers CHE-1900235 and CHE-2003685. TEM, XPS, and BET studies were performed as part of a user project at the National Center for Electron Microscopy and Molecular Foundry of Lawrence Berkeley National Laboratory, which is supported by the US Department of Energy.

Institutional Review Board Statement: Not applicable.

Informed Consent Statement: Not applicable.

Data Availability Statement: Data sharing is not applicable to this article. The data presented in this study are available on request from the corresponding author.

Conflicts of Interest: The authors declare no conflict of interest.

References

1. Ozoemena, K.I.; Chen, S. *Nanomaterials for Fuel Cell Catalysis*, 1st ed.; Nanostructure Science and Technology Series; Springer International Publishing: Cham, Switzerland, 2016; 583p. [CrossRef]
2. Wang, W.; Lei, B.; Guo, S.J. Engineering Multimetallic Nanocrystals for Highly Efficient Oxygen Reduction Catalysts. *Adv. Energy Mater.* **2016**, *6*, 1600236. [CrossRef]
3. He, G.Q.; Song, Y.; Liu, K.; Walter, A.; Chen, S.; Chen, S.W. Oxygen Reduction Catalyzed by Platinum Nanoparticles Supported on Graphene Quantum Dots. *ACS Catal.* **2013**, *3*, 831–838. [CrossRef]
4. Ustarroz, J.; Ornelas, I.M.; Zhang, G.H.; Perry, D.; Kang, M.; Bentley, C.L.; Walker, M.; Unwin, P.R. Mobility and Poisoning of Mass-Selected Platinum Nanoclusters during the Oxygen Reduction Reaction. *ACS Catal.* **2018**, *8*, 6775–6790. [CrossRef]
5. Niu, W.H.; Li, L.G.; Chen, S.W. Recent Progress in Template-Assisted Synthesis of Nitrogen-Doped Porous Carbons for Oxygen Electroreduction. *J. Electrochem.* **2017**, *23*, 110–122. [CrossRef]
6. Peng, Y.; Lu, B.Z.; Chen, S.W. Carbon-Supported Single Atom Catalysts for Electrochemical Energy Conversion and Storage. *Adv. Mater.* **2018**, *30*, 1801995. [CrossRef]
7. Wang, Y.X.; Su, H.Y.; He, Y.H.; Li, L.G.; Zhu, S.Q.; Shen, H.; Xie, P.F.; Fu, X.B.; Zhou, G.Y.; Feng, C.; et al. Advanced Electrocatalysts with Single-Metal-Atom Active Sites. *Chem. Rev.* **2020**, *120*, 12217–12314. [CrossRef]
8. Behan, J.A.; Mates-Torres, E.; Stamatin, S.N.; Dominguez, C.; Iannaci, A.; Fleischer, K.; Hoque, M.K.; Perova, T.S.; Garcia-Melchor, M.; Colavita, P.E. Untangling Cooperative Effects of Pyridinic and Graphitic Nitrogen Sites at Metal-Free N-Doped Carbon Electrocatalysts for the Oxygen Reduction Reaction. *Small* **2019**, *15*, 1902081. [CrossRef]
9. Wang, N.; Lu, B.Z.; Li, L.G.; Niu, W.H.; Tang, Z.H.; Kang, X.W.; Chen, S.W. Graphitic Nitrogen Is Responsible for Oxygen Electroreduction on Nitrogen-Doped Carbons in Alkaline Electrolytes: Insights from Activity Attenuation Studies and Theoretical Calculations. *ACS Catal.* **2018**, *8*, 6827–6836. [CrossRef]
10. Niu, W.H.; Li, L.G.; Liu, X.J.; Wang, N.; Liu, J.; Zhou, W.J.; Tang, Z.H.; Chen, S.W. Mesoporous N-Doped Carbons Prepared with Thermally Removable Nanoparticle Templates: An Efficient Electrocatalyst for Oxygen Reduction Reaction. *J. Am. Chem. Soc.* **2015**, *137*, 5555–5562. [CrossRef]
11. Lu, B.Z.; Smart, T.J.; Qin, D.D.; Lu, J.E.; Wang, N.; Chen, L.M.; Peng, Y.; Ping, Y.; Chen, S.W. Nitrogen and Iron-Codoped Carbon Hollow Nanotubules as High-Performance Catalysts toward Oxygen Reduction Reaction: A Combined Experimental and Theoretical Study. *Chem. Mater.* **2017**, *29*, 5617–5628. [CrossRef]
12. Liu, X.; Jiao, Y.; Zheng, Y.; Jaroniec, M.; Qiao, S.Z. Building up a Picture of the Electrocatalytic Nitrogen Reduction Activity of Transition Metal Single-Atom Catalysts. *J. Am. Chem. Soc.* **2019**, *141*, 9664–9672. [CrossRef] [PubMed]
13. Hou, C.C.; Zou, L.L.; Sun, L.M.; Zhang, K.X.; Liu, Z.; Li, Y.W.; Li, C.X.; Zou, R.Q.; Yu, J.H.; Xu, Q. Single-Atom Iron Catalysts on Overhang-Eave Carbon Cages for High-Performance Oxygen Reduction Reaction. *Angew. Chem. Int. Ed.* **2020**, *59*, 7384–7389. [CrossRef] [PubMed]
14. He, T.; Lu, B.Z.; Chen, Y.; Wang, Y.; Zhang, Y.Q.; Davenport, J.L.; Chen, A.P.; Pao, C.W.; Liu, M.; Sun, Z.F.; et al. Nanowrinkled Carbon Aerogels Embedded with FeNx Sites as Effective Oxygen Electrodes for Rechargeable Zinc-Air Battery. *Research* **2019**, *2019*, 6813585. [CrossRef] [PubMed]

15. Lu, B.Z.; Liu, Q.M.; Chen, S.W. Electrocatalysis of Single-Atom Sites: Impacts of Atomic Coordination. *ACS Catal.* **2020**, *10*, 7584–7618. [CrossRef]
16. Lefevre, M.; Proietti, E.; Jaouen, F.; Dodelet, J.P. Iron-Based Catalysts with Improved Oxygen Reduction Activity in Polymer Electrolyte Fuel Cells. *Science* **2009**, *324*, 71–74. [CrossRef]
17. Xiao, M.L.; Chen, Y.T.; Zhu, J.B.; Zhang, H.; Zhao, X.; Gao, L.Q.; Wang, X.; Zhao, J.; Ge, J.J.; Jiang, Z.; et al. Climbing the Apex of the ORR Volcano Plot via Binuclear Site Construction: Electronic and Geometric Engineering. *J. Am. Chem. Soc.* **2019**, *141*, 17763–17770. [CrossRef]
18. Mercado, R.; Wahl, C.; Lu, J.E.; Zhang, T.J.; Lu, B.Z.; Zhang, P.; Lu, J.N.Q.; Allen, A.; Zhang, J.Z.; Chen, S.W. Nitrogen-Doped Porous Carbon Cages for Electrocatalytic Reduction of Oxygen: Enhanced Performance with Iron and Cobalt Dual Metal Centers. *ChemCatChem* **2020**, *12*, 3230–3239. [CrossRef]
19. Chen, Y.; Hu, S.Q.; Nichols, F.; Bridges, F.; Kan, S.T.; He, T.; Zhang, Y.; Chen, S.W. Carbon aerogels with atomic dispersion of binary iron-cobalt sites as effective oxygen catalysts for flexible zinc-air batteries. *J. Mater. Chem. A* **2020**, *8*, 11649–11655. [CrossRef]
20. Yuan, S.; Cui, L.L.; Dou, Z.Y.; Ge, X.; He, X.Q.; Zhang, W.; Asefa, T. Nonprecious Bimetallic Sites Coordinated on N-Doped Carbons with Efficient and Durable Catalytic Activity for Oxygen Reduction. *Small* **2020**, *16*, 2000742. [CrossRef]
21. Sarkar, S.; Biswas, A.; Purkait, T.; Das, M.; Kamboj, N.; Dey, R.S. Unravelling the Role of Fe-Mn Binary Active Sites Electrocatalyst for Efficient Oxygen Reduction Reaction and Rechargeable Zn-Air Batteries. *Inorg. Chem.* **2020**, *59*, 5194–5205. [CrossRef]
22. Zhu, Z.J.; Yin, H.J.; Wang, Y.; Chuang, C.H.; Xing, L.; Dong, M.Y.; Lu, Y.R.; Casillas-Garcia, G.; Zheng, Y.L.; Chen, S.; et al. Coexisting Single-Atomic Fe and Ni Sites on Hierarchically Ordered Porous Carbon as a Highly Efficient ORR Electrocatalyst. *Adv. Mater.* **2020**, *32*, 2004670. [CrossRef] [PubMed]
23. Koshy, D.M.; Chen, S.C.; Lee, D.U.; Stevens, M.B.; Abdellah, A.M.; Dull, S.M.; Chen, G.; Nordlund, D.; Gallo, A.; Hahn, C.; et al. Understanding the Origin of Highly Selective CO_2 Electroreduction to CO on Ni,N-doped Carbon Catalysts. *Angew. Chem. Int. Ed.* **2020**, *59*, 4043–4050. [CrossRef] [PubMed]
24. Chen, S.C.; Koshy, D.M.; Tsao, Y.; Pfattner, R.; Yan, X.Z.; Feng, D.W.; Bao, Z.A. Highly Tunable and Facile Synthesis of Uniform Carbon Flower Particles. *J. Am. Chem. Soc.* **2018**, *140*, 10297–10304. [CrossRef] [PubMed]
25. Xing, Z.Y.; Qi, Y.T.; Tian, Z.Q.; Xu, J.; Yuan, Y.F.; Bommier, C.; Lu, J.; Tong, W.; Jiang, D.E.; Ji, X.L. Identify the Removable Substructure in Carbon Activation. *Chem. Mater.* **2017**, *29*, 7288–7295. [CrossRef]
26. He, T.; Peng, Y.; Jia, Q.X.; Lu, J.E.; Liu, Q.M.; Mercado, R.; Chen, Y.; Nichols, F.; Zhang, Y.; Chen, S.W. Nanocomposites Based on Ruthenium Nanoparticles Supported on Cobalt and Nitrogen-Codoped Graphene Nanosheets as Bifunctional Catalysts for Electrochemical Water Splitting. *ACS Appl. Mater. Interfaces* **2019**, *11*, 46912–46919. [CrossRef] [PubMed]
27. Liu, Q.M.; Peng, Y.; Li, Q.X.; He, T.; Morris, D.; Nichols, F.; Mercado, R.; Zhang, P.; Chen, S.W. Atomic Dispersion and Surface Enrichment of Palladium in Nitrogen-Doped Porous Carbon Cages Lead to High-Performance Electrocatalytic Reduction of Oxygen. *ACS Appl. Mater. Interfaces* **2020**, *12*, 17641–17650. [CrossRef] [PubMed]
28. He, T.; Zhang, Y.Q.; Chen, Y.; Zhang, Z.Z.; Wang, H.Y.; Hu, Y.F.; Liu, M.; Pao, C.W.; Chen, J.L.; Chang, L.Y.; et al. Single iron atoms stabilized by microporous defects of biomass-derived carbon aerogels as high-performance cathode electrocatalysts for aluminum-air batteries. *J. Mater. Chem. A* **2019**, *7*, 20840–20846. [CrossRef]
29. Morales, D.M.; Kazakova, M.A.; Dieckhofer, S.; Selyutin, A.G.; Golubtsov, G.V.; Schuhmann, W.; Masa, J. Trimetallic Mn-Fe-Ni Oxide Nanoparticles Supported on Multi-Walled Carbon Nanotubes as High-Performance Bifunctional ORR/OER Electrocatalyst in Alkaline Media. *Adv. Funct. Mater.* **2020**, *30*, 1905992. [CrossRef]
30. Liu, C.; Li, H.; Chen, J.S.; Yu, Z.X.; Ru, Q.; Li, S.Z.; Henkelman, G.; Wei, L.; Chen, Y. 3d Transition-Metal-Mediated Columbite Nanocatalysts for Decentralized Electrosynthesis of Hydrogen Peroxide. *Small* **2021**, *17*, 2007249. [CrossRef]
31. Grosvenor, A.P.; Kobe, B.A.; Biesinger, M.C.; McIntyre, N.S. Investigation of multiplet splitting of Fe 2p XPS spectra and bonding in iron compounds. *Surf. Interface Anal.* **2004**, *36*, 1564–1574. [CrossRef]
32. Grosvenor, A.P.; Biesinger, M.C.; Smart, R.S.; McIntyre, N.S. New interpretations of XPS spectra of nickel metal and oxides. *Surf. Sci.* **2006**, *600*, 1771–1779. [CrossRef]
33. Zhong, H.X.; Wang, J.; Zhang, Q.; Meng, F.L.; Bao, D.; Liu, T.; Yang, X.Y.; Chang, Z.W.; Yan, J.M.; Zhang, X.B. In Situ Coupling FeM (M = Ni, Co) with Nitrogen-Doped Porous Carbon toward Highly Efficient Trifunctional Electrocatalyst for Overall Water Splitting and Rechargeable Zn-Air Battery. *Adv. Sustain. Syst.* **2017**, *1*, 1700020. [CrossRef]
34. Cheng, Y.; He, S.; Veder, J.P.; De Marco, R.; Yang, S.Z.; Jiang, S. Atomically Dispersed Bimetallic FeNi Catalysts as Highly Efficient Bifunctional Catalysts for Reversible Oxygen Evolution and Oxygen Reduction Reactions. *ChemElectroChem* **2019**, *6*, 3478–3487. [CrossRef]